Journal of Physics:
Conference Series

PAPER • OPEN ACCESS

Wind tunnel measurement on a wind turbine blade tip with flush-mounted MEMS pressure and acoustic sensors

To cite this article: Nan Hu *et al* 2026 *J. Phys.: Conf. Ser.* **3224** 042065

Journal of Physics: Conference Series **3224** (2026) 042065 doi:10.1088/1742-6596/3224/4/042065

Wind tunnel measurement on a wind turbine blade tip with flush-mounted MEMS pressure and acoustic sensors

Nan Hu[1], Arnaud Le Floc'h[1], Alexandre Suryadi[1], Michaela Herr[1], Daniel Ernst[2], Armin Goudarzi[2], Ferdinand Popp[3], Richard Czuberny[3], Philipp Mühlmann[3] and Jörg Meyer[3]

[1]Wind Energy Department, Institute of Aerodynamics and Flow Technology, German Aerospace Center (DLR), Braunschweig, Germany

[2]Experimental Methods Department, Institute of Aerodynamics and Flow Technology, German Aerospace Center (DLR), Göttingen, Germany

[3]Transport Aircraft Department, Institute of Aerodynamics and Flow Technology, German Aerospace Center (DLR), Braunschweig, Germany

E-mail: nan.hu@dlr.de

Abstract. Over 200 pressure Micro-Electro-Mechanical Systems (MEMS) sensors and more than 1000 acoustic MEMS sensors were installed on a wind turbine tip model with a length of 1995 mm and a root chord length of 826 mm. Measurements were conducted in the closed test section of the Low-Speed Wind Tunnel DNW-NWB in Braunschweig, with test velocities ranging from 40 to 70 m/s and geometric angles of attack between –7° and 25°. Flow transition was detected using infrared thermography, while wall shear stress at the trailing-edge region was measured with capacitive shear stress sensors, and flow velocity was obtained with a pressure rake. The MEMS measurements clearly identified key flow characteristics, such as flow transition and flow separation.

1. Introduction

Accurate knowledge of the local angle of attack (AOA) of the blade, as well as key flow characteristics such as flow transition and flow separation, are essential for ensuring highly efficient operation of wind turbines. Although turbine loads and overall behavior result from aerodynamic phenomena, system validation and turbine control are generally based on integral quantities such as power, rotational speed, or bending moments. This limitation arises from the lack of suitable aerodynamic sensors and the associated data processing capabilities. Such sensors must be robust, weatherproof, and installed with minimal disturbance to the flow. Moreover, real-time data processing that evaluates the major flow characteristics is required to enable efficient turbine control.

Recently, Barber et al. [1] developed a wireless Micro-Electro-Mechanical Systems (MEMS)-based pressure and acoustic measurement system, which was applied to airfoils in wind tunnel tests. The collected data were used to infer the AOA through stagnation point detection with differential pressure sensors near the leading edge, a method shown to be effective in a wind tunnel campaign using a 2D NACA0018 airfoil. Additionally, an approach for identifying leading edge erosion, based on instantaneous snapshots of the measured pressure fields, was demonstrated using CFD data. This system, including a photovoltaic energy harvester with a rechargeable battery holder, was later installed on the

Journal of Physics: Conference Series **3224** (2026) 042065 doi:10.1088/1742-6596/3224/4/042065

blade of a 6 kW wind turbine [2]. MEMS sensors were placed at the leading edge and on the suction side of the trailing edge to enable aerodynamic monitoring on operating wind turbines.

With the recent advances in machine learning applied to flow dynamics, real-time processing for evaluating the AOA and key flow characteristics has become feasible. Yilmaz and Bekemeyer [3] proposed a transfer learning framework using convolutional neural networks to predict onflow parameters from sparse surface pressure data, such as real-time data measured by MEMS sensors. This approach improves prediction accuracy through domain adaptation and shows potential for practical wind turbine monitoring applications. Stahl et al. [4] investigated flow separation detection using machine learning methods and demonstrated high prediction accuracy with a support vector machine (SVM) model, which utilizes wall pressure spectra rather than time series to enable real-time detection.

This paper presents a MEMS-based pressure measurement system applied to a wind turbine blade, suitable for both aerodynamic and aeroacoustic analyses [5]. The novel measurement technique enables the characterization of flow dynamics over a large measurement area without introducing significant flow disturbances, thanks to the small size and low cost of the sensors. The analysis focuses on revealing key flow characteristics, such as flow transition and flow separation, which are critical to wind turbine operating efficiency. The medium-term objective of this research is the prototypical deployment of the system at the DLR WiValdi wind park.

2. Model instrumentation and measurement setup

A wind turbine blade tip model was tested in the closed test section of the Low-Speed Wind Tunnel DNW-NWB in Braunschweig, see Fig. 1(a). The wind tunnel is an atmospheric, closed-circuit facility with a test section size of 3.25 m width and 2.8 m height, which can also be operated with an open test section. The maximum free stream velocity in the closed test section is 90 m/s. The turbulence intensity in the closed test section is smaller than 0.06%.

The model was a tip part of an original EU 51 MS wind turbine blade. Due to the balance limit of DNW-NWB, the blade was cut to a height of 1995 mm, which has a chord length of 826 mm at the root. Significant effort was devoted to refining the blade's surface finish and incorporating recessed areas for MEMS installation flush with the surface.

To measure the static and dynamic pressures, pressure MEMS (pMEMS) and acoustic MEMS (aMEMS) on specially designed printed circuit boards (PCB) [6, 7] were surface-flush-mounted in recesses at the leading and trailing edge regions on both sides of the blade. The model was equipped with 288 pMEMS sensors (BOSCH BMP 390), of which 256 were installed on the mid-height section via 8 PCB patches, each carrying 32 sensors, illustrated in Fig. 1(b). The tip was equipped with 32 pressure tabs, which were connected via tubes to two 16-channel MEMS pressure scanners. The pressure scanner's sensors are the same type as those on the PCBs. To increase spatial resolution at the leading edge, pressure tabs were spaced in the streamwise direction with slightly offset spanwise positions. At the mid-height section of the model, two parallel PCBs were installed, with a half-PCB sensor spacing shift at the leading edge. For data recording, dedicated interface modules were established to connect the PCBs and pressure scanners to the data acquisition computer. These modules supply power to the devices and enable communication between the sensors and the computer, ensuring proper system operation and data transfer. During the measurements, the pMEMS signals were recorded at a sampling rate of 100 Hz.

There were 23 aMEMS patches, each assembled with 48 MEMS microphones (IM72D128V01), flush-mounted on the blade. In addition to linearly distributed sensors along the chord next to the pMEMS, an aMEMS array was instrumented on both the suction and pressure sides at the trailing edge region, enabling separation of hydrodynamic and acoustic pressures in the wavenumber domain. The aMEMS patches were connected to a Field Programmable Gate Array (FPGA) based data acquisition system within the model, which sent the raw sensor data via a network cable to a server outside the model. All FPGAs received the same 3.072 MHz clock from a single source, ensuring phase-aligned measurements across all MEMS microphones. The raw pulse-density modulation stream, which is 1 bit at 3.072 MHz, is then converted to a 32-bit pulse-code modulation stream at 48 kHz by a four-stage

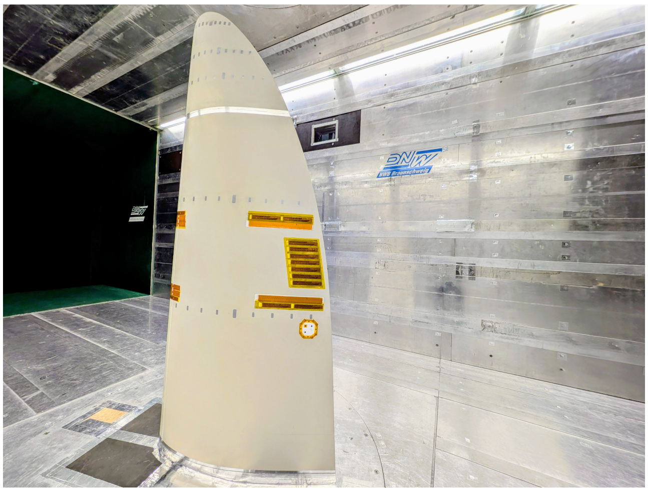

(a)

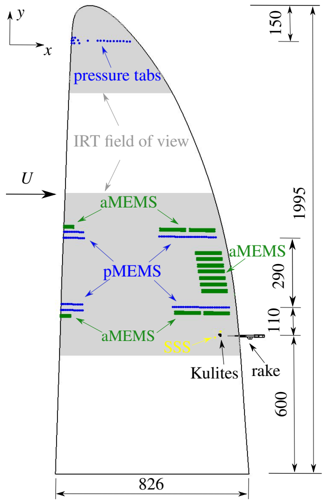

(b)

Figure 1: (a) Photograph of test setup in the closed test section of NWB; (b) Schematic sketch of the suction side of the model with dimensions in mm.

decimation filter on the server's graphics card.

The acquisition software of both p/aMEMS was triggered via a transistor-transistor logic signal from the wind tunnel, ensuring synchronized measurements between the wind tunnel and MEMS systems. The data recording time was 10 s. A live data stream was delivered to external computers for real-time online predictions of C_p over the whole blade, free-stream flow velocity, AOA, and flow separation status with machine learning methods [8, 9].

Lastly, for the model instrumentation, a pair of IC2 shear stress capacitive sensors (SSS), along with three Kulite sensors, were installed in a disk with a diameter of 68 mm below the aMEMS patch on the suction side at the trailing edge region, as shown in Fig. 1(a). The shear stress sensors are composed of a 2mm x 0.4mm micromachined floating element sensor that enables time-resolved direct measurements of both the mean and fluctuating components of shear stress. The mean value can be used to determine whether the flow is attached (positive sign) or separated (negative sign). The Kulites are used to validate the aMEMS results and study the link between wall pressure and shear stress with synchronized measurements.

To detect the laminar-turbulent transition and assess the impact of flush-mounted MEMS on flow transition, three infrared thermography (IRT) cameras were installed outside the wind-tunnel wall behind small openings. One InfraTec VarioCam HD 800 (+30mm lens) and one FLIR SC3000 (+ 20° lens) were focused on the mid-height section of the model on the suction and pressure sides, respectively, covering the MEMS area from the leading to trailing edge. A second FLIR SC3000 was used to focus on the tip region on the suction side.

Furthermore, a pressure rake consisting of 32 tubes (5 faulty tubes) with a 3 mm spacing between adjacent tubes was connected to MEMS pressure scanners with the same sensor type as those installed on the blade, allowing measurements at a sampling rate of 100 Hz over a 10 s recording time. The rake was mounted on an approximately 600 mm long support bar fixed to the rotation disk, allowing it to rotate together with the model. Two positions were measured with the rake. Both were located at the same height, 80 mm below the lowest linearly distributed aMEMS sensors. In the streamwise direction, one position was 50 mm upstream of the trailing edge, while the other was 15 mm downstream of the trailing edge.

Journal of Physics: Conference Series **3224** (2026) 042065 doi:10.1088/1742-6596/3224/4/042065

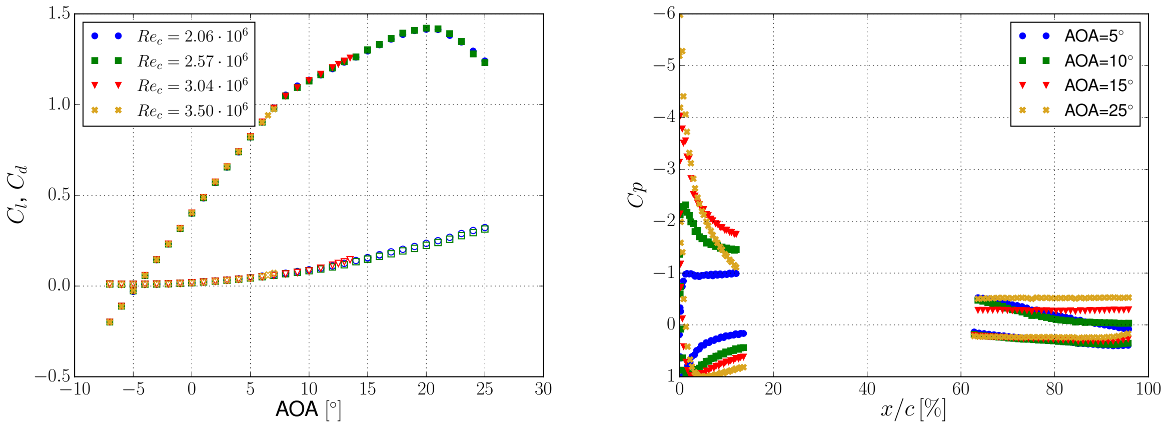

(a) (b)

Figure 2: (a) Lift and drag of the blade model; (b) C_p distribution for selected AOAs with $U_\infty = 50$ m/s.

3. Results

3.1. Flow conditions

The tested flow velocities U_∞ were between 40 m/s and 70 m/s, and the geometric AOA ranged from -7° to 25° for $U_\infty = 40$ m/s and 50 m/s, covering conditions from negative lift to blade stall. For the higher velocities, the maximum AOA was reduced according to the wind-tunnel balance limit of lift. Clean (non-tripped) and with zigzag strip tripped configurations were tested. Due to the page limit, only the results of the clean configuration are discussed in this paper.

Fig. 2(a) shows the lift (C_l) and drag (C_d) coefficients measured with the balance for the clean configuration. The C_l result indicates that flow separation occurred at the trailing edge along a large spanwise portion of the blade at AOA $\geq 9°$, characterized by a reduced slope of the lift increase against AOA. A stall occurs at AOA$> 20°$, from which C_l falls. The minimum C_d was measured at AOA=-5° where $C_l \simeq 0$. At AOA>-5°, C_d increases slowly with an increasing AOA, and the increase rate becomes more significant for AOA $\geq 9°$ where flow separation occurred on the model.

Fig. 2(b) shows the C_p distribution of both suction and pressure sides at the bottom pMEMS patch position for selected AOAs, where x/c denotes the chordwise coordinate normalized by the chord length. At the suction side of the leading edge, C_p decreases with an increasing AOA, and reaches $C_p \simeq$ -6 for a stall condition at AOA=25°. After reaching the minimum, C_p increases towards the trailing edge and recovers to approximate zero for AOA=5° and 10°. For AOA=15° and 25°, a plateau of C_p was measured at $x/c > 63\%$, which results from the flow separation at the whole rear portion. Furthermore, a small portion of C_p (from $x/c \simeq 90\%$) shows a flat distribution for AOA=10°, indicating a possible separation occurring close to the trailing edge.

For the stall condition at AOA=25°, C_p increases at the leading edge region significantly faster compared to the case of AOA= 15°, and reaches $C_p \simeq$ -1 at $x/c = 12\%$. If C_p remains constant for the rest of the chord length behind the onset of flow separation, i.e. $C_p \simeq$ -0.5 for the AOA=25% case, we may assume that the onset of separation is located at approximately $x/c = 20\%$ for this stall case.

Fig. 3(a) shows the mean velocity profiles, estimated based on the pressure rake measurement. The required local static pressure was provided from the pMEMS sensor, positioned at the same x/c but 110 mm above the rake measurement point, see Fig. 1(b). The result shows that the boundary layer thickness δ increases from approximately 16 mm for AOA=5° up to 48 mm for AOA=10°. At an AOA of 5°, the flow remains attached. However, a separated boundary layer was observed at AOA $\geq 10°$, which is consistent with the trends seen in the C_p distribution. The separation was identified by regions

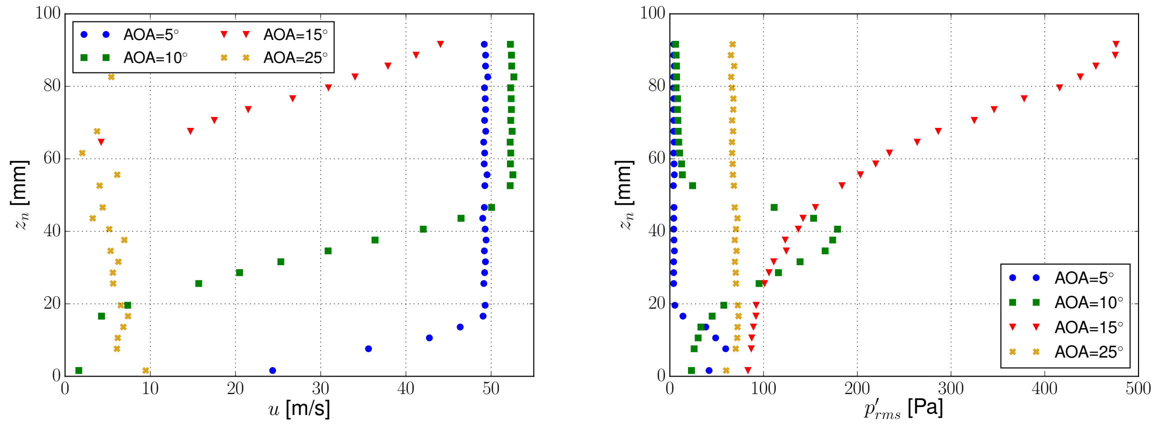

(a) (b)

Figure 3: Rake results for selected AOAs with $U_\infty = 50$ m/s at $x/c = 93\%$ as a function of surface-normal distance, (a) Mean velocity profiles; (b) p'_{rms} profiles.

where the measured total pressure was lower than the static pressure, i.e., $y < 16$ mm for AOA = 10° and $y < 65$ mm for AOA = 15°. This occurs because backflow in the recirculation zone generates suction at the tube, resulting in a measured pressure below the static pressure [10]. Furthermore, for AOA = 25°, the entire measurement region lies within the wake behind the recirculation zone, as indicated by the aMEMS results. In this wake region, turbulence with high intensity and a significant yaw angle causes the tube to be strongly misaligned with the local flow direction, introducing significant uncertainty in the estimated velocity measurements [11].

Fig. 3(b) shows the RMS values of the measured pressure fluctuations, which can reflect the trend of the Reynolds stress component $\overline{u'_1 u'_1}$. Abe [12] performed direct numerical simulations of a flat-plate flow with separation and reattachment, and showed profiles of p' and turbulence kinetic energy (TKE) across the boundary layer at upstream positions and within the separation bubble. These cases represented mild and strong adverse pressure gradients as well as flow separation. In all cases, the profiles of p' and TKE showed comparable trends. Consequently, the peak value of p'_{rms} in the field measured with the rake identifies the position of maximum TKE, which moves farther from the wall as the adverse pressure gradient increases, i.e., with increasing AOA. As with the mean velocity results, the estimated p'_{rms} values can have considerable uncertainty in the recirculation region.

3.2. Leading edge region

A significant feature of the flow in practice is the flow transition on the suction side of the wind turbine blade. Fig. 4 shows the infrared results on the suction side for the selected AOAs. Flow transition can be identified at $x/c \simeq 50\%$ for AOA=5°, evidencing that the installed MEMS had a negligible effect on the flow at this condition and did not trigger flow transition. The transition location moved toward the leading edge as AOA increased. Due to thermal conduction effects of the PCB patches, a flow transition in the patch area cannot be identified. At large AOAs, i.e. 15° and 25°, a thin dark line was measured, indicating a laminar separation bubble (LSB) because the local convective heat-transfer coefficient is significantly reduced by a laminar bubble's quasi-static recirculating flow [13].

Fig. 5 shows the p'_{rms} development of wall pressure fluctuations at the leading edge region measured by aMEMS. According to the aMEMS sensor datasheet, it has a flat frequency response (± 1 dB) from 50 Hz to 13 kHz. Therefore, if significant wall pressure fluctuations occur at frequencies outside this range, they could introduce uncertainty into the obtained p'_{rms} value. The results indicate that flow

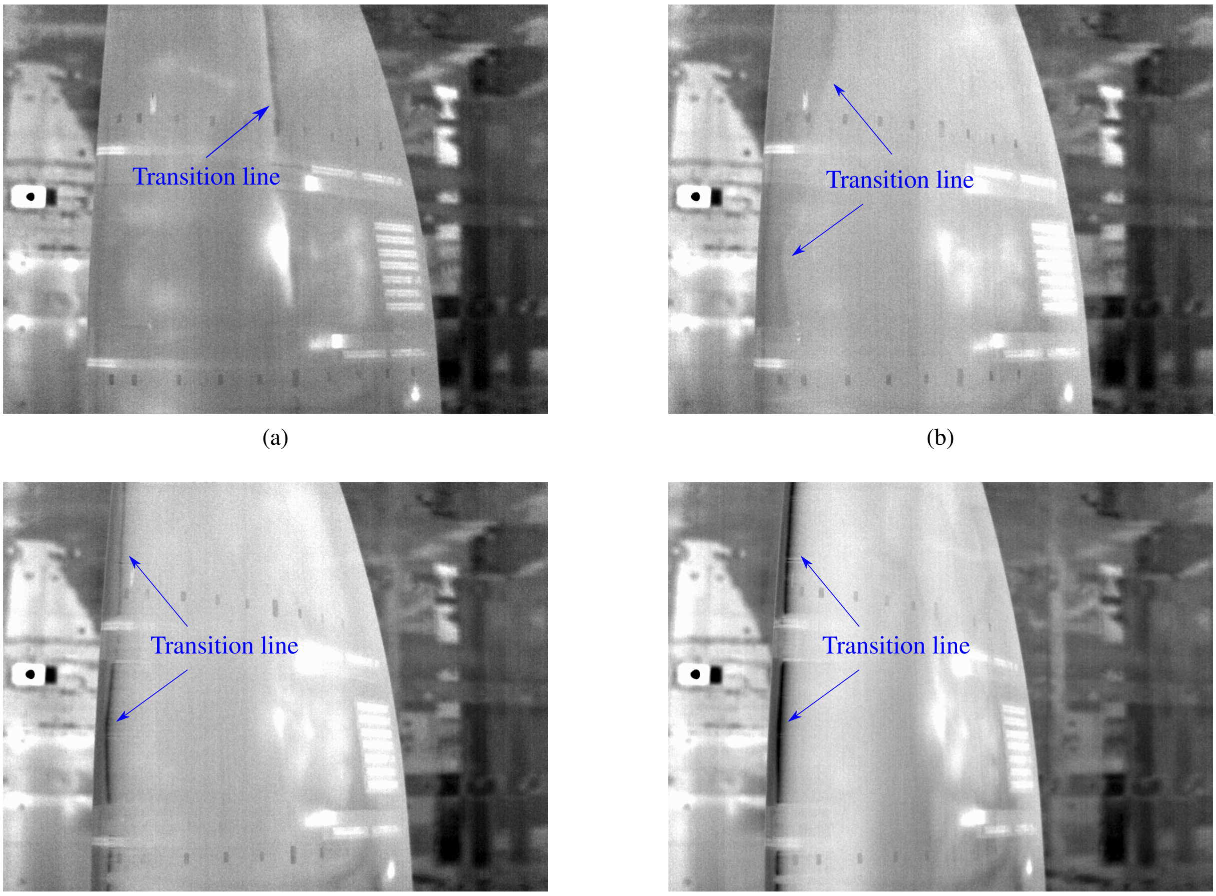

(a) (b) (c) (d)

Figure 4: Infrared results for $U_\infty = 50$ m/s, (a) AOA=5°; (b) AOA=10°; (c) AOA=15°; (d) AOA=25°.

transtion starts at $x/c > 6\%$, $x/c \simeq 4.2\%$, $x/c \simeq 2.4\%$ and $x/c \simeq 1.0\%$ for AOA=5°, 10°, 15° and 25°, respectively, characterized by an increase of p'_{rms}. Note that the increase of p'_{rms} at $x/c = 3.8\%$ for AOA=5° and 10° is due to a faulty frequency response of the sensor at frequencies lower than 2 kHz, see Figs. 6(a,b). For laminar flows, the value of p'_{rms} is significantly smaller than that in turbulent flows. Furthermore, a peak in intermittency of p'_{rms} was measured in the transition region for AOA=15° and 25°, which results from LSB. Note, that due to significant sensor overload at $x/c = 1.5\%$ for the AOA=25° case, no useful time series were recorded. Therefore, the p'_{rms} value at this position, which represents the expected peak value for the AOA=25° case, cannot be determined. Downstream of the peak intermittency, the p'_{rms} value falls and reaches a relatively constant level corresponding to turbulent flows. It is believed that, for AOA=10° without an LSB, a peak intermittency also occurs, as reported by [14, 15]. This is because $p'_{rms} > 100$ Pa was measured at $x/c = 5.6\%$ for AOA=10°, which is significantly larger than the values observed for AOA=15° and 25°, representing the fully developed turbulent flow. The p'_{rms} values in the turbulent flow for AOA=10° are expected to be lower than in these cases, due to the significantly smaller local flow velocity indicated by the C_p distribution, see Fig. 2(b). Furthermore, due to the significant difference in the local velocities at the leading edge for different AOAs, the p'_{rms} value varies considerably for laminar flow conditions, as shown in Fig. 5.

Fig. 6 shows the power spectral density (PSD) measured by aMEMS at selected streamwise positions. The spectra presented in this paper were calculated using a Hanning window with 4096 samples per

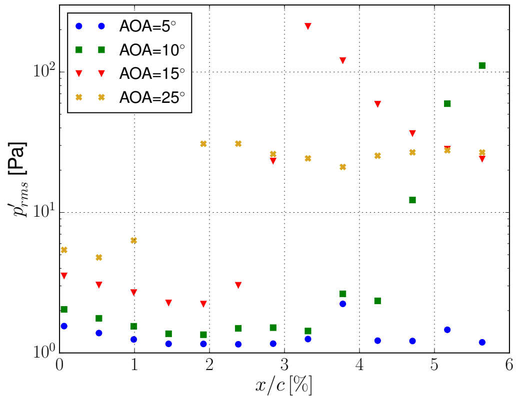

Figure 5: p'_{rms} at the leading edge region on the suction side for $U_\infty = 50$ m/s.

window and 50% overlap, giving a resolution of 11.7 Hz. For AOA=5°, the laminar flow has a low wall pressure level, as shown in Fig. 6(a). However, small peaks at approximately 2.5 kHz, 5.7 kHz and 15.5 kHz were measured, and likely correspond to the onset of Tollmien–Schlichting (TS) waves. Significantly stronger TS waves were measured by aMEMS at the leading edge region for AOA=10° with multiple peaks between 5 kHz and 16 kHz. For AOA=15°, a hump peaking at 17 kHz was measured, and is probably caused by vortex shedding of LSB. Indeed, the estimated $St = fL/U_0 \simeq 1.6$ aligns with measured value of $St \simeq 1.7$ and 2.0 of velocity spectra from literature [16, 17]. Note that the estimate of the characteristic length L of the LSB may involve some uncertainties. For the literature cases, L is estimated based on the LSB size from contour plots, whereas in the present case, it is determined from the length of the black line in the infrared results. Interestingly, a pronounced hump with a peak exceeding 100 dB appeared at AOA=15°, which was absent in the stall case at AOA=25°. Unfortunately, due to significant overload, the time series around $x/c = 1.5\%$ is completely distorted, and the corresponding spectrum cannot be calculated or displayed.

3.3. Trailing edge region

Flow separation is a significant phenomenon in practice, leading to both lift loss and increased noise emission. The measured wall shear stress shows a negative value at AOA $\geq 10°$, as shown in Fig. 7. This negative value is caused by the backward flow in the recirculating region, which indicates flow separation [18]. Because the measurement position was at $x/c = 90\%$, flow separation occurring directly at the trailing edge should be at an even smaller AOA, consistent with the C_l result shown in Fig. 2(a). Furthermore, the wall shear stress exhibits a sudden drop at AOAs of 7°, 6° and 5° for $Re_c = 2.06 \cdot 10^6$, $Re_c = 2.57 \cdot 10^6$ and $Re_c > 3 \cdot 10^6$, respectively. This sudden drop is attributed to a significant shift in the flow transition position, which moves noticeably toward the leading edge. The transition is caused by disturbances induced by the discontinuity between the MEMS patch and the model surface, resulting in a wedge-shaped region that significantly affects shear stress results.

The p'_{rms} results between $x/c = 65\% - 95\%$, shown in Fig. 8, indicate that as the AOA increases up to 15°, the p'_{rms} value increases within the measured area. This is due to the flow encountering a more pronounced adverse pressure gradient upstream for a larger AOA. However, at an AOA of 25°, the p'_{rms} value drops significantly compared to the 15° case, reaching levels similar to those observed at 5°. It is worth noting that the aMEMS sensor's frequency response shows a drop in sensitivity below 50 Hz, with attenuation reaching approximately 3 dB at 20 Hz and increasing rapidly as the frequency decreases further. Therefore, the actual p'_{rms} values, particularly in the region of separated flow, are likely to be somewhat higher than the measured values, as separated flow typically contains more energy at lower

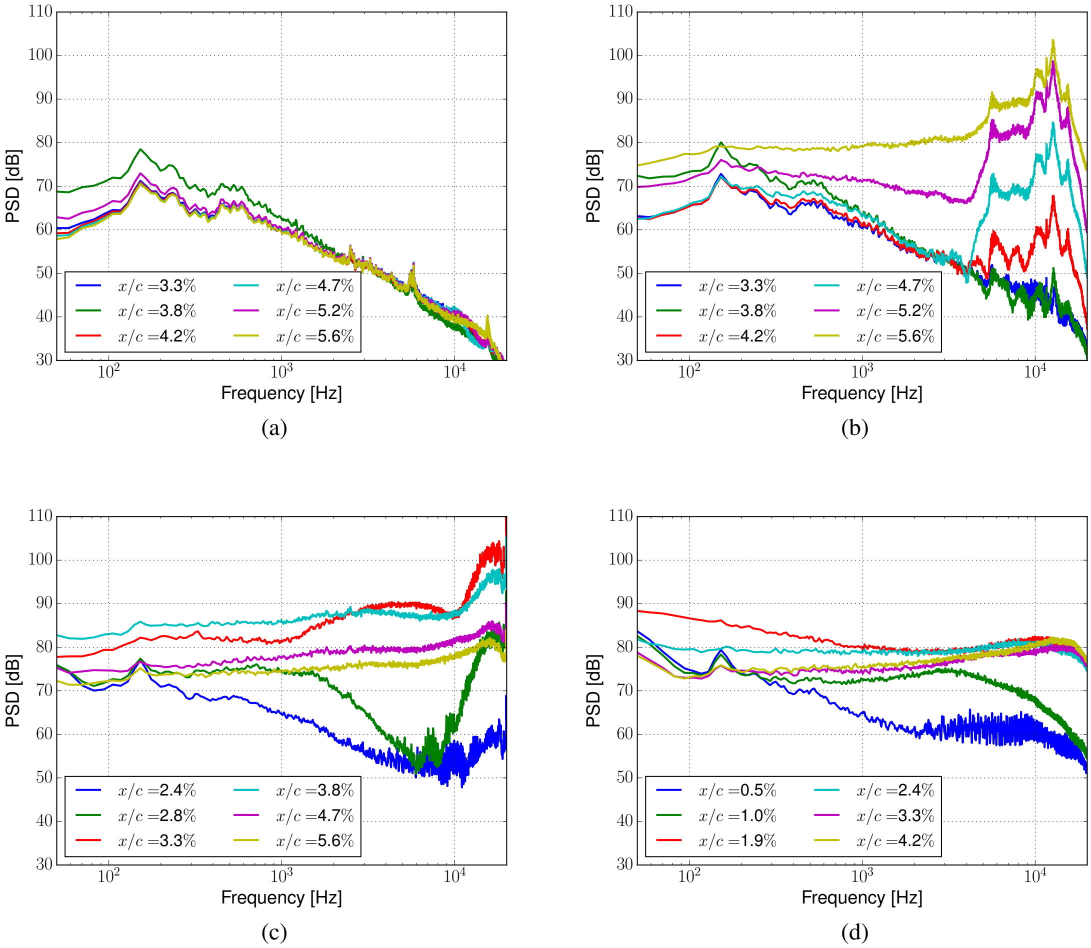

Figure 6: Wall pressure spectra at the leading edge region on the suction side for $U_\infty = 50$ m/s, (a) AOA=5°; (b) AOA=10°; (c) AOA=15°; (d) AOA=25°.

frequencies.

Fig. 9 shows the autospectra measured by aMEMS at selected positions between $x/c = 65\%$-95%. For AOA=5°, the flow remains attached across the entire measurement region. The spectral peak level increases as the position moves toward the trailing edge, and the mid-frequency slope above 1 kHz becomes steeper. This is attributed to the longer exposure to the adverse pressure gradient [19]. As the AOA increases to 10°, flow separation onset is expected to occur at $x/c \leq 90\%$, as indicated by the shear stress results (see Fig. 7). The measured spectra show a distinct kink between 1-1.5 kHz at positions $x/c = 88\%$ and 94%, which is caused by flow separation, indicating that the measurement points lie within the recirculation region [18, 20]. The spectra in separated flows are influenced by two major sources: i) vortex shedding at the outer boundary layer, which contributes to the low-frequency hump, and ii) the recirculation region, which is the dominant source of high frequencies above the kink frequency. For AOA=15°, the kink appears at all measured positions due to the expansion of the recirculation region. Additionally, the peak level increases further, and the peak frequency shifts to a lower value compared to the 10° case. As the AOA further increases to 25°, the kink disappears at $x/c > 76\%$. This is probably because the onset of flow separation occurs much farther toward the leading edge, along with the recirculation region. Positions closer to the trailing edge are likely located in the

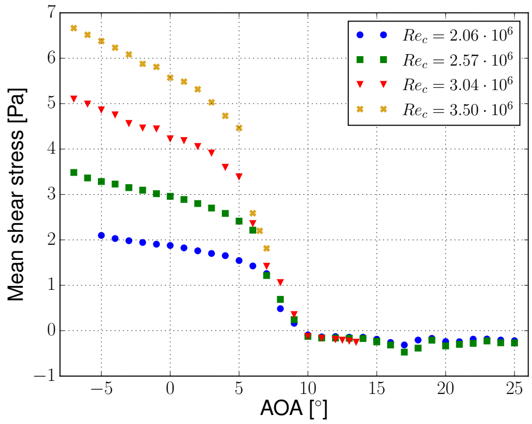

Figure 7: Mean wall shear stress at $x/c = 90\%$ on the suction side.

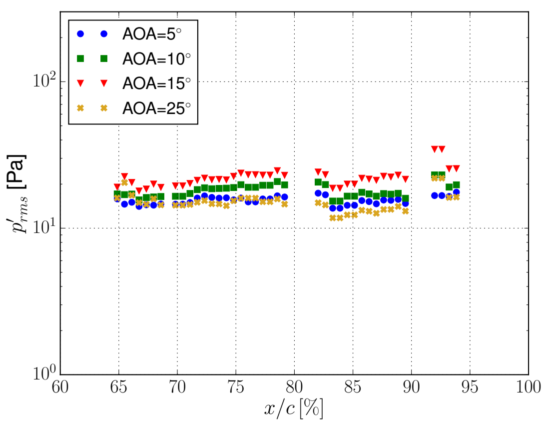

Figure 8: p'_{rms} at the trailing edge region on the suction side for $U_\infty = 50$ m/s.

wake downstream of the recirculation region, leading to a different wall-pressure spectral shape than in the separated region.

4. Conclusion

A wind turbine blade tip model, with a height of 1995 mm and a chord length of 826 mm at the root, was tested in the closed test section of the Low-Speed Wind Tunnel DNW-NWB. The free-stream velocity ranged from 40 m/s to 70 m/s, with the AOA varying from -7° to 25°. PCB patches containing over 200 pMEMS sensors and 1000 aMEMS sensors were installed in recesses on the model surface at the leading and trailing edge regions, at mid-height. One of the main objectives of this installation was to explore the potential for detecting flow transition and separation using MEMS sensors. To identify flow transition, IRT was conducted and a pair of shear stress sensors were placed at the trailing edge region to validate flow separation. Additionally, boundary layer velocities were measured using a pressure rake with a pressure scanner, positioned directly behind the shear stress sensors.

Results for the non-tripped case at four selected AOAs with a free-stream velocity of 50 m/s were analyzed. The major findings are summarized as follows:

- Based on p'_{rms} of wall pressure measured by aMEMS, the flow transition could be identified, which was further validated by IRT results.
- At AOA=15°, an LSB was detected in the IRT measurements, and the vortex shedding associated with the LSB was clearly reflected in the wall pressure spectra measured by the aMEMS sensors, consistently with literature cases.
- The wall pressure spectra measured in the trailing edge region can be used to identify flow separation, which is characterized by a distinct kink in the medium-frequency range. Frequencies below this kink are mainly associated with vortex shedding in the outer boundary layer, whereas the higher-frequency components are attributed to backflow close to the wall. The flow-separation condition determined from the wall-pressure spectra is also fully consistent with that identified using the shear stress sensor measurements.
- At AOA=25°, p'_{rms} at the trailing-edge region decreases significantly compared with the case at 15°. In addition, no distinct kink is observed in the wall pressure spectra at positions close to the trailing edge, indicating that these locations lie in the wake downstream of the recirculation region.
- The pressure rake can be used to identify flow separation when the velocity cannot be determined within the recirculation region, as the measured pressure falls below the static pressure due to

Journal of Physics: Conference Series **3224** (2026) 042065 doi:10.1088/1742-6596/3224/4/042065

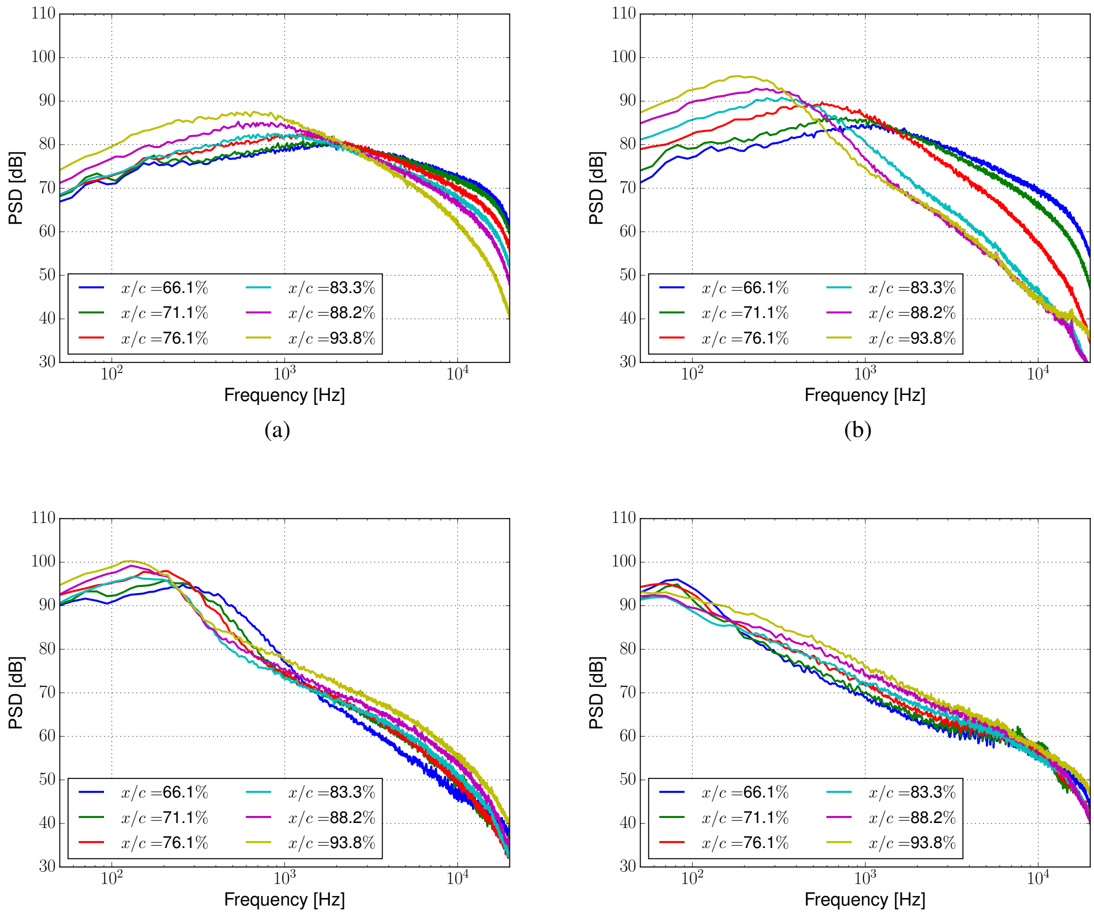

(a) (b) (c) (d)

Figure 9: Wall pressure spectra at the trailing edge region on the suction side for $U_\infty = 50$ m/s, (a) AOA=5°; (b) AOA=10°; (c) AOA=15°; (d) AOA=25°.

backflow. Furthermore, the acquired p'_{rms} reflects the distribution trend and the peak location of TKE within the boundary layer.

Overall, this study demonstrated that the applied MEMS can capture important aerodynamic characteristics of a wind turbine blade, such as flow transition and flow separation. Building on this potential, future work will explore practical applications of the sensors, including tests planned at the DLR WiValdi wind park.

Acknowledgments

This work is financed by the DLR Impulse Project SAFER2. The authors sincerely thank the DNW-NWB wind tunnel team for their excellent support throughout the measurement campaign.

References

[1] Barber S, Deparday J, Marykovskiy Y, Chatzi E, Abdallah I, Duthé G, Magno M, Polonelli T, Fischer R and Müller H 2022 Development of a wireless, non-intrusive, mems-based pressure and

acoustic measurement system for large-scale operating wind turbine blades *Wind Energ. Sci.* **7** 1383–1398

[2] Polonelli T, Moallemi A, Kong W, Müller H, Deparday J, Magno M and Benini L 2023 A self-sustainable and micro-second time synchronized multi-node wireless system for aerodynamic monitoring on wind turbines *IEEE Access* **11** 119506–119522

[3] Yilmaz E and Bekemeyer P 2026 Predicting onflow parameters using transfer learning for domain and task adaptation *Aerospace Science and Technology* **168** 1–19

[4] Stahl K, Le Floc'h A, Pester B, Ebert P L, Suryadi A, Hu N and Herr M 2025 Toward the detection of flow separation for operating airfoils using machine learning *Int. J. Turbomach. Propuls. Power* **10** 1–21

[5] Goudarzi A, Ahlefeldt T, Ernst D, Geisler R, Philipp F, Hu N and Spehr C 2026 Measurements of dynamic surface pressure field on a wind turbine blade with acoustic MEMS *32nd AIAA/CEAS Aeroacoustics Conference*

[6] Raab C and Rohde-Brandenburger K 2021 Dynamic flight load measurements with mems pressure sensors *CEAS Aeronautical Journal* **12** 737–753

[7] Ernst D, Goudarzi A, Geisler R, Philipp F, Ahlefeldt T and Spehr C 2024 Enhancing aeroacoustic wind tunnel studies through massive channel upscaling with MEMS microphones *AIAA Paper 2024-3064* 1–16

[8] Yilmaz E and Bekemeyer P 2025 Transfer learning approach to predicting operating conditions during wind tunnel tests *AIAA Paper 2025-3588* 1–21

[9] Pester B, Le Floc'h A, Philipp F and Hu N 2026 Real-time detection of flow separation using machine learning: a proof of concept study *TORQUE Conference 2026*

[10] Mojola O O 1978 Pitot-tubes at 90 and 180 degrees of yaw *Aeronaut. J.* **82** 355–357

[11] Barlow J B, Rae W H and Pope A 1999 *Low-speed wind tunnel testing* (John Wiley & Sons)

[12] Abe H 2017 Reynolds-number dependence of wall-pressure fluctuations in a pressure-induced turbulent separation bubble *J. Fluid Mech.* **833** 563–598

[13] Ricci R and Montelpare S 2005 A quantitative ir thermographic method to study the laminar separation bubble phenomenon *Int. J. Therm. Sci.* **44** 709–719

[14] Casper K M, Beresh S J, Henfling J F, Spillers R W, Pruett B and Schneider S P 2009 Hypersonic wind-tunnel measurements of boundary-layer pressure fluctuations *AIAA Paper 2009-4054* 1–20

[15] Richter K, Koch S, Gardner A, Mai H, Klein A and Rohardt C H 2014 Experimental investigation of unsteady transition on a pitching rotor blade airfoil *J. Am. Helicopter Soc.* **59(1)** 1–12

[16] Borgmann D, Hosseinverdi S, Little J and Fasel H 2025 Experimental and numerical investigations of transition in a pressure-gradient-induced laminar separation bubble *J. Fluid Mech.* **1007** 1–30

[17] Ducoin A and Astolfi J A 2019 Wall-pressure fluctuations of laminar separation bubble based on direct numerical simulation and experiments over a hydrofoil at re = 450,000 *European Journal of Mechanics / B Fluids* **76** 132–144

[18] Le Floc'h A, Suryadi A, Hu N, Herr M, Wang S, Ghaemi S, Vétel J, Di Labbio G and Dufresne L 2024 Wall pressure signature of separated flows: A comparison between flat plate and airfoil *13th International Symposium on Turbulence and Shear Flow Phenomena* 1–6

[19] Hu N 2018 Empirical model of wall pressure spectra in adverse pressure gradients *AIAA Journal* **56** 3491–3506

[20] Suryadi A and Herr M 2015 Wall pressure spectra on a du96-w-180 profile from low to pre-stall angles of attack *AIAA Paper 2015-2688* 1–18